Title

POLARIZATION AND DIFFERENTIAL CROSS SECTIONS IN PROTON-PROTON-NUCLEUS SCATTERING AT 725 MeV

Authors

McManigal, Paul G.
Eandi, Richard D.
Kaplan, Selig N.
et al.

Publication Date

1964-08-01

UCRL-11496

University of California

Ernest O. Lawrence Radiation Laboratory

POLARIZATION AND DIFFERENTIAL CROSS SECTIONS
IN PROTON-PROTON AND PROTON-NUCLEUS SCATTERING AT 725 MeV

Berkeley, California

DISCLAIMER

For
Phys. Rev.

UCRL-11496

UNIVERSITY OF CALIFORNIA

Lawrence Radiation Laboratory
Berkeley, California

AEC Contract No. W-7405-eng-48

POLARIZATION AND DIFFERENTIAL CROSS SECTIONS IN PROTON-PROTON AND PROTON-NUCLEUS SCATTERING AT 725 MeV

Paul G. McManigal, Richard D. Eandi, Selig N. Kaplan, and
Burton J. Moyer

August 11, 1964

Polarization and Differential Cross Sections In Proton-Proton and Proton-Nucleus Scatterings at 725 MeV*

Paul G. McManigal,† Richard D. Eandi, Selig N. Kaplan, and Burton J. Moyer

Lawrence Radiation Laboratory
University of California
Berkeley, California

August 11, 1964

ABSTRACT

The polarization and angular distribution of protons scattered from protons, helium, beryllium, carbon, aluminum, calcium, iron, and tantalum were measured as functions of angle at 725 MeV. A variation of the usual double-elastic-scattering method was used, in that the sense of the first scattering angle was reversed in finding asymmetries rather than the second angle. Energy analysis of the scattered beam was accomplished by means of a 102-degree magnetic spectrometer allowing a total resolution of ±10 MeV. The data were fitted with an optical model. In the proton-nucleus scattering the polarization reaches a maximum value of about 40% at angles less than the diffraction minimum. Results in proton-proton scatterings are more interesting; however, because of an uncertainty in the analyzing power of the carbon, a definitive statement cannot be made. This can be said, however: either the polarization in proton-proton scatterings is above 50% at this energy or the analyzing power of carbon at 6 deg at 600 MeV is more than 40%, which is considerably greater than the 30% measured at 725 MeV.

I. INTRODUCTION

The study of nucleon scattering at high energies by nucleons and nuclei has provided a considerable body of information about the nature of the nuclear force. In simple terms, total cross section measurements yield information on the strength of the interaction, whereas differential cross section measurements reveal details of the nuclear forces' radial dependence. However, it takes a study of polarization phenomena to determine the role of the nucleon's spin in the interaction.

The employment and comparative success of the optical model in describing first, cross sections[1] and later, polarizations[2] of nucleons in high energy nucleon-nucleus collisions is well known. Theoretical and experimental work prior to 1960 have been reviewed by Squires.[3]

This experiment is an attempt to repeat at 725 MeV the extensive survey performed by Chamberlain et al.[4] at 310 MeV and to fit the experimental observations with an optical model. The target materials used were the same as those in the 310-MeV experiment (namely He, Be, C, Al, Ca, Fe, and Ta). The optical-model formalism used in fitting the data has been adapted from Batty.[5] Polarization and cross section measurements in pp scattering are also reported.

II. EXPERIMENTAL METHOD

The polarization produced by high-energy scattering is generally studied by double scattering. Scattering an unpolarized nucleon beam by a target produces a polarized beam. This polarization can be measured by scattering from a second target, producing an azimuthal asymmetry in the intensity which is given by

$$I(\theta_2, \phi) = I_0(\theta_2) \left[1 + P_1(\theta_1) A_2(\theta_2) \cos \phi\right] ,$$

where I_0 is the intensity for unpolarized protons, $P_1(\theta_1)$ is the polarizing power of the first target, $A_2(\theta_2)$ is the analyzing power of the second scattering, and ϕ is the azimuthal angle between planes of the first and second scattering.[4] By sampling the relative intensity at ϕ equal to 0 and 180 deg, we may simply evaluate the asymmetry

$$\epsilon(\theta_2) = P_1(\theta_1) A_2(\theta_2) = \frac{I(\theta_2, 0°) - I(\theta_2, 180°)}{I(\theta_2, 0°) + I(\theta_2, 180°)} .$$

If both the first and second targets are the same and both scatterings elastic, with the angles of scattering and the incident energies nearly equal, the asymmetry is the square of the polarization. (By time reversal, for elastic scatterings, the analyzing power is equal to the polarizing power.) The elasticity of each scattering can be ensured by imposing an energy requirement after the scatterings by range or magnetic analysis. Once the polarizing or analyzing power of a target for a particular angle of scattering has been established, then other polarization measurements may be made by changing one of the target materials or angles of scattering and again measuring the asymmetry.

At proton energies of several hundred MeV, ensuring the elasticity is a difficult problem. Since the energy lost in exciting the nucleus a few MeV is a very small part of the initial energy of the proton, only by using the most elaborate magnetic analysis can one detect the difference between elastically and near-elastically scattered particles. Such a magnetic analyzing system needs space and power, and considerable care must be exercised to ensure that solid angles involved remain constant for the left and right scatterings. Great practical advantage is gained by not requiring magnetic analysis on both the left and right side of the second scatterer. Varying the sense of the first scattering angle and holding the second fixed yields an asymmetry which is theoretically equivalent to varying the second and holding the first fixed. By fixing the angle of scattering after the second target, we can use a single magnetic system. Also, certain systematic errors are reduced by such a second-angle-constant system. If the beam is monitored at the second target, the asymmetry reflects, in the first approximation, the polarizing power of the first target and the analyzing power and differential cross section at the second target.[6] Since polarization varies more slowly with angle than the differential cross section, the results are much more sensitive to changes in alignment at the second target than at the first target. Keeping this second angle constant greatly reduces potential alignment error.

The magnet system external to the cyclotron shielding is shown in Fig. 1. This compound system can be decomposed into three units. The first unit contained two bending magnets with opposite fields which steered the beam through the first target at a given angle. In the second unit was a lead collimator and a quadrupole triplet. The third unit, the spectrometer, was composed of four bending magnets with a focusing quadrupole in the center. This system provided

a 102-deg magnetic spectrometer having a dispersion of 1 MeV/cm at the final focus position.

The angle of scattering at the second target was fixed at 6 deg because it was estimated to best fit the following criteria: (a) a large ratio of elastically scattered protons from carbon and helium to inelastically scattered protons to minimize inelastic contamination, (b) a large value for the product of $I(\theta)P(\theta)^2$ to minimize statistical errors, and (c) large polarization to minimize systematic errors. (Before the experiment, the proton-carbon polarization at 6 deg was estimated on the basis of previous work to be about 50%.[5,7])

As seen in Fig. 1, the angle θ_1 was defined by the collimator, the position of the first target, and an ion chamber with a split signal foil. The current from both halves of this split ion chamber were monitored by electrometers and balanced on a zero-centered recording potentiometer. The position of the scattered beam was monitored by a similar split-foil ion chamber, θ_2, which was located behind the second target, T_2, and defined the line connecting T_1 and T_2 through the center of the collimation. The proton beam was aligned by adjusting the currents in the first two bending magnets until null readings were obtained in both split ion chambers. The beam that passed through the first and second targets was monitored with ion chambers. The angular resolution in the scattering angles was due to geometric definition and multiple scattering in the targets. The combination amounted to about 0.5 deg rms error for all elements at both targets, with the exception of tantalum, in which case this value was slightly greater than 1 deg.

The particles scattering from the first and second targets at the proper angles and passing through the spectrometer were monitored by the scintillation counter coincidence $M_1M_2M_3$. M_1 and M_2 were small counters placed

between T_2 and the entrance collimator of the spectrometer. M_3 was a large scintillator, 12 in. high by 24 in. wide, at the focus of the spectrometer. A horizontal profile of the beam at the spectrometer focus was obtained with six smaller scintillators ($S_1 \cdots S_n \cdots S_6$) that subtended adjacent 2-in. widths in the center of M_3. A continuous beam profile was obtained by coincidence of the form $(M_1M_2M_3)S_n$. It was found that with the scattered beam centered in the profile scintillators the elastic peak could be essentially all contained in the four center ones (Fig. 2). Furthermore, the total counts in this peak varied negligibly with the slight magnet drifts. It proved most convenient to monitor these "peak" counts with an additional scintillation coincidence, $(M_1M_2M_3)S_p$, where S_p was an 8-in.-wide scintillator that exactly covered the areas of the four central small counters, $S_2S_3S_4S_5$. Asymmetries were determined from the ratios of numbers of particles registering in the peak or large counters to those passing through the second-target ion chamber, for both left and right scatterings at the first target.

The most important polarization measurement is the one in which the analyzing power of the second target is established. The use of helium as an analyzer is conceptually pleasing because of its lack of excited states. However, comparison of the energy distribution of the protons scattered at 6 deg by carbon at both targets with that of protons scattered by helium at both targets showed no evidence of near-elastic scattering at 6 deg. Because of the convenience gained by working with a target that is solid at room temperatures, this double-carbon 6-deg scattering was then accepted as a standard for the experiment and was repeated more than 20 times and under different test conditions. The test measurements showed that polarization was not detectably affected by different

beam shapes, beam intensities, beam spills, or target thicknesses. The system was further checked by comparing measurements when both targets were hydrogen, helium, beryllium, or aluminum with measurements where either target was replaced by carbon. All measurements were consistent. The agreement in the case of helium and carbon will be found along with the helium data in Table II. Most asymmetries were measured with helium as an analyzer. To increase counting rates, carbon was generally used as an analyzer for hydrogen and helium, and for scattering, at 10 and 13 deg, from the solid targets. The analyzing power of carbon at 6 deg was found to be 0.300 ± 0.003, and that of helium was 0.333 ± 0.003. Since all polarization measurements were reproducible to within their statistical errors, and there was no reason to suspect a constant systematic error, the errors reported with the data are those due to statistics.

The lab energy of the proton beam at the first target was about 735 MeV. Except for hydrogen, which is discussed later, the lab energy was about 715 MeV at the second target. Thus 725 MeV was chosen as the reported energy. Except for hydrogen, polarization values were not considered to be energy-dependent.

An additional check was accomplished by double-scattering alpha particles. Since the alphas have no spin, any measured asymmetry would reflect a bias in the experiment. This check is much more sensitive to misalignment, since the differential cross section varies much more rapidly with angle for α particles than it does for protons. Alignment of the alpha beam was less certain that that of the proton beam, because of the lower flux of particles. Despite these problems, the asymmetry was found to be $1.5 \pm 1.5\%$, which we considered and treated as zero.

Differential cross-section data were obtained as a byproduct of the polarization measurements. Perhaps the largest error in the differential-cross-section measurements came through use of collimators rather than counters to define

solid angles. No allowance for collimator scattering has been made. The ratio of the counters to the first ion chamber was reproducible to about ±5%. The statistical error was always less than 1%.

The ratio of the flux C in the $(M_1M_2M_3)S_p$ or $M_1M_2M_3$ counters to the flux F in the first target ion chamber, is proportional to a product of elastic plus near-elastic differential cross sections, $d\sigma/d\Omega$, at the two targets

$$(C/F)_{ave} = \frac{d\sigma}{d\Omega_1} \frac{d\sigma}{d\Omega_2} d\Omega_1 d\Omega_2 \rho_1 \rho_2 ,$$

where $d\Omega$ and ρ are respectively the appropriate solid angle and target density normalizing factors. Since a product of cross sections is involved, answers obtained from this latter method reflect only one-half of whatever constant systematic errors there may have been.

III. EXPERIMENTAL RESULTS

1. Protons on Hydrogen

The measured asymmetries for protons polarized on hydrogen and analyzed by carbon are given in Table I (Column b). For hydrogen there is, of course, no problem in separating out inelastic events, since there are none below meson threshold. However, because of kinematic energy loss in proton-proton scatterings the energy of the protons arriving at the carbon analyzer varies over a considerable range. In order to separate out the properties of protons one must know the energy dependence of both the carbon cross section and carbon analyzability. The proton kinetic energy at the carbon analyzer is given in Table I (Column c). Some experimental values of differential cross sections and polarizations for proton scattering

at 6 deg from carbon are given in Fig. 3. The polarization results, although unfortunately sparse, indicate that there are either experimental discrepancies or considerable fluctuations with energy in the p-C polarization. We have arbitrarily sketched the dashed lines in Fig. 3b to suggest a possible envelope of values for this p-C polarization. If we assume the values on curve A, Fig. 3, we obtain the p-p polarizations tabulated in Table I (Column d). The curve B gives the values in Table I(Column e). On the basis of our present knowledge, and without additional information, the two sets of values must be considered as experimental limits. Both these sets of values are given in Fig. 4.

In Fig. 5 is plotted maximum p-p polarization as a function of energy. The smooth variation of this function gives more credence to the curve B (Fig. 3b), at least in the energy range between 600 and 715 MeV, and therefore to the polarizations of Table I (Column e).

Unfortunately, we cannot make definitive statements about the above measurements; however, we can say that either $P_{pp}(\theta)$ is high at this energy, or $A_{p\text{-}C}(6 \text{ deg})$ rises sharply with decreasing energy.

With regard to the differential cross sections, we have assumed $d\sigma/d\Omega\,|_{p\text{-}C}$ at 6 deg to be a constant and equal to our measured value at 725 MeV. The assumption here is based on the apparent constancy of the total p-C elastic cross section[5] -- a simple square-well optical-model calculation indicated that, in the energy range of interest ($\approx$ 600 to 700 MeV), $d\sigma/d\Omega\,|_{p\text{-}C}$ at 6 deg is nearly proportional to the total elastic cross section.

2. Protons on Helium

The differential cross section and polarization for protons scattering from helium are listed in Table II and plotted in Fig. 6. Only in the hydrogen and helium

measurements do near-elastics not distort the polarization and differential-cross-section measurements. The features are similar to the data at 310 MeV.[4]

3. Protons on Other Elements

The beryllium and carbon data are given in Table III and plotted in Figs. 7 and 8. At small angles, the beryllium and carbon polarization data look quite similar to the helium data. From the energy profile at the final counters for the measurements at 10 and 13 deg, it was apparent the results are an average over near-elastic states and are not to be interpreted as elastic measurements. An elastic polarization, which closely follows that of the helium polarization as the angle approaches the classical diffraction minimum, is not inconsistent with these measurements. The differential-cross-section results can be interpreted as only an upper limit for the elastic differential cross section at the larger angles.

The data for the heavier elements are also found in Table III and plotted on Figs. 9 through 12. The most striking feature of the polarization measurements are that they are so similar at the same laboratory angle. Near-elastics also contaminate the results whenever the elastic-diffraction minimum is approached. The angular resolution in the measurements of the heavier elements suffers because of multiple scattering. Because of these effects, fine details of the scatterings are unobservable. This is particularly true for tantalum.

IV. OPTICAL MODEL FITTING

The differential cross sections and polarization from helium, beryllium, carbon, aluminum, calcium, iron, and tantalum were analyzed by fitting the experimental data with an optical model. In this model, the nucleus is represented by a complex potential well of the form[5]

$$V(r) = V_e \rho'(r) - |V_c| e^{i\theta_c} \rho(r) + |V_s| e^{i\theta_s} \frac{\hbar}{\mu c} \frac{d}{dr} \rho(r) \underline{\sigma} \cdot \underline{L} ,$$

where V_e is the Coulomb potential arising from the charge distribution $\rho'(r)$, and $\rho(r)$ is the nuclear matter distribution, and $|V_c| e^{i\theta_c}$ and $|V_s| e^{i\theta_s}$ are the complex central and spin-orbit potential strengths respectively. The imaginary part of the central nuclear potential can be related to the mean nucleon-nucleon total cross section $\bar{\sigma}$ for the incident protons by[19]

$$\text{Im } V_c(r) = \frac{k}{ZE} A \bar{\sigma} \rho(r) ,$$

where E is the total energy of the proton in the proton-nucleus c.m. system, k is its c.m. momentum, and A is the atomic number of the target particle. The nuclear density has been normalized to unit volume integral

$$\int_0^\infty \rho(r) 4\pi r^2 dr = 1$$

and

$$\bar{\sigma} = [Z\sigma_{pp} + (A - Z)\sigma_{pn}]/A .$$

Using the optical model, Batty has completed a comprehensive work on the subject of scatterings of high-energy nucleons by carbon.[5] He has solved for radii and potentials, using carbon experiments from 95 to 970 MeV incident proton energies. The data of this experiment were analyzed along the lines of Batty's formulation of the optical model.

For the nuclear distributions, the same shapes as found by Hofstadter in electron-scattering experiments were used.[20] For the light elements, a modified Gaussian was used:

$$\rho(r) = \left[1 + f\,\frac{4}{3}\left(\frac{r}{a_1}\right)^2\right]\exp\left[-(r/a_1)^2\right] .$$

Here the value of f determines the shape of the nuclear distribution and a_1 determines its size. For helium f was taken to be zero, reducing the distribution to a pure Gaussian. For beryllium f was set to 1/2 and for carbon f was 1. The Fermi shape

$$\rho(r) = \frac{1}{1 + e^{\left[(r - r_0)/a\right]}}$$

was also used for carbon and for the heavier elements. Here r_0 is the radius at half-height and a determines the thickness of the edge of the nucleus. To relate potentials with different radial forms, Feshbach suggests integrating over the volume of the nucleus and comparing results for the integral[21]

$$I(V) = \int_0^\infty V(r)\, 4\pi r^2 dr .$$

When the modified Gaussian was used, the charge density was assumed to have the same distribution as the nuclear distribution. When the Fermi model was used, the trapezoidal form

$$\rho'(r) = 1, \quad \text{for } r < (r_0 - 2.75\,a),$$

$$\rho'(r) = \frac{(r_0 + 2.75\,a) - r}{5.5\,a}, \quad \text{for } (r_0 - 2.75\,a) < r < (r_0 + 2.75\,a),$$

$$\rho'(r) = 0, \quad \text{for } r > (r_0 + 2.75\,a)$$

was used for the charge distribution.[20] The advantage here was that this form was analytically integrable. Its use is justified by the good approximation it makes to to the Fermi model and also because the Coulomb effect is relatively unimportant at this energy.

In fitting the experimental data with the optical-model potential, an IBM 7090 computer program was used. This program started with the potential in terms of $|V_c|$, θ_c, $|V_s|/|V_c|$, and $(\theta_c-\theta_s)$, and with radial values for a_1 and f for fitting the modified Gaussian, or r_0 and a for fitting the Fermi form. From these, it generated values of the polarization as well as the differential, total, and absorption cross section. These values were compared with the corresponding experimental values and χ^2 was computer. The program then varied any or all of the first five of these parameters in a grid manner, attempting always to reduce χ^2. Uniqueness is determined by starting the program at different initial values. The data are fitted well by several choices of the phase of the central potential θ_c. The solution with a large positive imaginary central potential and a small negative real central potential fits the data as well as any. In addition, Batty shows this solution to fit nicely with measurements at other energies.[5] Two families of solutions correspond to $\sin(\theta_c-\theta_s)$ in either the first or second quadrant. The corresponding imaginary part of the spin-orbit potential is positive and negative, respectively. The positive solution fits the helium data better. Combining this with the showing that at lower energies the real part of the spin-orbit potential is to be positive, we took the positive solution to be the correct one.

When the modified Gaussian was used for fitting the data on the light elements, the value of the radius a_1 was allowed to vary; f, a, and r_0 were fixed at the values obtained by electron scattering. Because of the absence of near-elastic scattering contaminating the helium data, the potential values found in fitting these data are judged most reliable. In fitting the beryllium and carbon data, the data from only the first four angles were used because of the high percentage of contamination from near-elastic states at larger angles. For carbon, in addition to the angular distribution and polarization data, the total and absorption cross sections were used.[22-25]

For the heavier elements, the average proton-nucleon cross section $\bar{\sigma}$ and the ratio of the real to imaginary central potential were fixed at the carbon values. Only the spin-orbit potential was allowed to vary. Data from only the first three angles were used. A search was not made for tantalum, but the average value of $\bar{\sigma}$ and the ratio of all potentials were held fixed. The values of the potential and related parameters are given in Table IV. The errors on the potentials are crudely estimated by seeing how χ^2 varied as these parameters changed. The computed differential cross sections and polarization are plotted along with the data on Figs. 6 through 12. The fit with the data appears good when allowance is made for near-elastic scattering and angular resolution. The central potential is seen to be mostly imaginary and the real part small and negative. The phase of the spin-orbit potential is close to that of the central potentials. This reflects the low values of the polarization. The predictions of the modified Gaussian and Fermi models for proton-carbon scattering were similar; those of the modified Gaussian are plotted in Fig. 8.

ACKNOWLEDGMENTS

The authors would like to express their appreciation to Dr. Robert W. Kenney and Dr. Vincent Z. Peterson for their invaluable contributions to the experimental setup and run, even while simultaneously doing measurements of their own in the polarized beam. Thanks are also due to Mr. Charles Chiu for his help during the experimental run, and to Mrs. Barbara Levine for her assistance with the optical-model fitting program.

The efforts of Mr. James T. Vale and the cyclotron crew to provide us with the clean, well-focused external proton beam is gratefully acknowledged.

Dr. C. J. Batty promptly and patiently communicated suggestions to us until we were able to reproduce his results with his data and our computer program. The criticisms by Dr. Owen Chamberlain of various schemes for measuring polarization were most helpful.

FOOTNOTES AND REFERENCES

*This work was supported by the U.S. Atomic Energy Commission.

†Present address: Aeronutronic Division, Ford Motors, Newport Beach, California.

1. S. Fernbach, R. Serber, and T. B. Taylor, Phys. Rev. 75, 1352 (1949).
2. E. Fermi, Nuovo Cimento 11, Ser. 9, 407 (1954).
3. E. J. Squires, Progr. Nucl. Phys. 8, 47 (1960).
4. O. Chamberlain, E. Segrè, R. D. Tripp, C. Wiegand, and T. Ypsilantis, Phys. Rev. 102, 1659 (1956).
5. C. J. Batty, Nucl. Phys. 23, 562 (1961).
6. A detailed error analysis of this technique can be found in Paul G. McManigal (Thesis), Lawrence Radiation Laboratory Report UCRL-10637 1963 (unpublished).
7. M. G. Mescheriakov, S. B. Nurushev, and G. D. Stoletov, Zh. Eksperim. i Teor. Fiz. 31, 361 (1956); Soviet Phys. JETP 4, 337 (1957).
8. J. Dickson and D. C. Salter, Nuovo Cimento 6, 235 (1957).
9. R. Alphonce, A. Johansson, and G. Tibell, Nucl. Phys. 3, 185 (1957).
10. W. G. Chesnut, E. M. Hafner, and A. Roberts, Phys. Rev. 104, 449 (1956).
11. E. Heiberg, Phys. Rev. 106, 1271 (1957).
12. Yu. Akimov, O. Savchenko, and L. Soroko, Zh. Eksperim. i Teor. Fiz. 35, 89 (1958).
13. L. S. Azhgirey, Yu. P. Kumekin, M. G. Mescheryakov, S. B. Nurashev, G. D. Stoletov, and Huang De-Tsang, Nucl. Phys. 43, 213 (1963).
14. A. E. Taylor and E. Wood, Nucl. Phys. 25, 642 (1961).
15. J. Tinlot and R. E. Warner, Phys. Rev. 124, 890 (1961).
16. O. Chamberlain, E. Segrè, R. D. Tripp, C. Wiegand, and T. Ypsilantis, Phys. Rev. 105, 288 (1957).

17. J. A. Kane, R. A. Stallwood, R. B. Sutton, T. H. Fields, and J. G. Fox, Phys. Rev. 95, 1694 (1954).

18. R. J. Homer, W. K. McFarlane, A. W. O'Dell, E. J. Sacharidis, and G. H. Eaton, Nuovo Cimento 23, 690 (1962).

19. W. Riesenfeld and K. Watson, Phys. Rev. 102, 1157 (1956).

20. R. Hofstadter, Ann. Rev. Nucl. Sci. 7, 231 (1957); R. Herman and R. Hofstadter, High-Energy Electron Scattering Tables (Stanford University Press, Stanford, 1960).

21. H. Feshbach, Ann. Rev. Nucl. Sci. 8, 49 (1958).

22. Moskalev et al. (reference 23) measured the absorption cross section for 650-MeV protons on carbon to be 227±12 mb. Booth et al. (reference 24) found the value 220±18 mb for 765-MeV neutrons on carbon. The value 225±10 mb was used in our program. For the total cross section, Booth et al. measured 342.1±3.7 mb, and Dzhelepov et al. (reference 25) measured 319±2 mb for 590-MeV neutrons. We used a value of 330±10 mb.

23. V. I. Moskalev and B. V. Bavrilovskii, Doklady Akad. Nauk SSSR 110, 972 (1956).

24. N. E. Booth, G. W. Hutchinson, and B. Ledley, Proc. Phys. Soc. (London) 71, 293 (1958).

25. V. P. Dzhelepov, V. I. Satarov, and B. M. Golovin, Soviet Phys. JETP 2, 349 (1956).

Table I. Differential cross sections and polarizations for proton-proton scattering. Column b gives the measured asymmetry of the beam after analysis with carbon; column c the proton energy at the carbon analyzer, and columns d and e the calculated p-p polarizations based on two different assumptions for the energy dependence of p-C polarization, as indicated.

	(a)	(b)	(c)	(d)	(e)
θ_{lab} (deg)	$(d\sigma/d\Omega)_{lab}$ [a] (mb/sr)	Asymmetry analyzing with carbon	Energy at the center of T_2 (MeV)	Polarization [Curve A of Fig. 3b used for A_{pC}(6 deg]	Polarization [Curve B of Fig. 3b used for A_{pC}(6 deg]
4.5	57.9	0.075±.004	718	0.250	0.246
6.0	55.7	0.107±.004	713	0.354	0.340
7.3	51.3	0.118±.003	708	0.392	0.369
8.6	46.2	0.129±.004	703	0.431	0.391
10.0	45.3	0.145±.003	694	0.483	0.433
11.5	38.5	0.166±.004	684	0.553	0.481
13.0	37.7	0.172±.002	674	0.572	0.485
15.3	31.7	0.185±.002	655	0.609	0.493
16.4	26.5	0.196±.004	645	0.652	0.516
18.0	25.2	0.198±.003	631	0.661	0.495
20.5	19.7	0.200±.003	605	0.666	0.482

a. These numbers have a reproducibility error of ±5% plus an additional error due to uncertainty in the energy dependence of the p-C cross section at 6 deg, see text.

Table II. Differential cross section and polarization for protons scattering from helium.

θ_{lab} (deg)	$(d\sigma/d\Omega)_{lab}$ (mb/sr) Elastic	Including 30-MeV loss	Polarization
4.5	360	366	0.280±.012
6.0[a]	280	291	0.332±.005
6.0[b]	273	288	0.339±.005
6.1	260	267	0.328±.008
7.3	200	210	0.369±.011
8.6	145	152	0.393±.011
10.0	96.0	103	0.423±.010
11.5	55.4	61.1	0.413±.013
13.0	31.5	35.1	0.439±.018
13.0	32.5	39.4	0.446±.018
15.3	10.6	12.9	0.348±.033
16.4	5.4	7.0	0.265±.043
18.0	2.0	2.7	0.132±.072

[a] Both targets helium

[b] Carbon at the first target, helium at the second

Table III. Differential cross sections and polarization for proton scattering from various nuclei.

θ_{lab} (deg)	$(d\sigma/d\Omega)_{lab}$(mb/sr) Including 15 MeV loss	Including 30 MeV loss	Polarization
	Beryllium		
4.0	1320	1390	0.217±.007
5.0	951	1005	0.267±.007
6.0	640	692	0.316±.007
7.3	381	428	0.368±.008
8.6	223	266	0.411±.012
10.0	137	169	0.395±.010
13.0	41	60	0.452±.025
	Carbon		
4.0	2120	2210	0.233±.005
5.0	1500	1580	0.265±.005
6.0	970	1040	0.300±.003
7.3	520	570	0.348±.006
8.6	250	300	0.369±.009
10.0	116	148	0.335±.015
13.0	33	50	0.445±.028
	Aluminum		
4.0	5480	5730	0.212±.006
5.0	3150	3320	0.250±.008
6.0	1510	1640	0.275±.007
7.3	491	577	0.326±.013
8.6	147	215	0.383±.022
10.0	95.3	144	0.443±.021
13.0	51.8	78.6	0.531±.030
	Calcium		
4.0	7690	8040	0.205±.006
5.0	3680	3900	0.246±.008
6.0	1360	1505	0.278±.009
7.3	324	424	0.362±.019
8.6	142	259	0.416±.027
10.0	174	237	0.497±.020
	Iron		
4.0	10080	10550	0.187±.006
5.0	3910	4170	0.215±.011
6.0	1113	1270	0.211±.011
7.3	285	386	0.369±.026
8.6	292	380	0.447±.024
10.0	245	308	0.403±.018
	Tantalum		
4.0	13600	14300	0.164±.011
5.0	5980	6370	0.185±.011
6.0	2870	3130	0.266±.011
7.3	1440	1610	0.349±.018
8.6	570	707	0.365±.023
10.0	339	434	0.444±.023

Table IV. Optical-model parameters

Element	Model	$\lvert V_c \rvert$ (MeV)	θ_c (deg)	$\lvert V_s \rvert / \lvert V_c \rvert$	$(\theta_c - \theta_s)$ (deg)	Re V_c (MeV)	Im V_c (MeV)	Re V_s (MeV)	Im V_s (MeV)
He	Gaussian	63 ± 4	97 ± 10	0.052 ± .004	23 ± 2	- 7.6	62.2	0.90	3.14
Be	Mod. Gauss.	48 ± 3	100 ± 10	0.037 ± .004	27 ± 8	- 8.4	47.6	0.53	1.69
C	Mod. Gauss.	49 ± 3	100 ± 10	0.035 ± .004	26 ± 4	- 8.4	48.2	0.48	1.64
C	Fermi	56 ± 3	100 ± 10	0.035 ± .004	27 ± 4	- 9.6	55.2	0.59	1.86
Al	Fermi	54.8	100[a]	0.030 ± .004	29 ± 4	- 9.5	54.0	0.53	1.58
Ca	Fermi	51.1	100[a]	0.021 ± .004	46 ± 4	- 8.9	50.3	0.63	0.89
Fe	Fermi	53.2	100[a]	0.026 ± .004	31 ± 4	- 9.2	52.4	0.51	1.29
Ta	Fermi	46.0	100[a]	0.035[a]	27[a]	- 8.0	45.3	0.47	1.54

Element	Model	$I(\mathrm{Re}V_c)/A$	$I(\mathrm{Im}V_c)/A$	$\lvert I(\mathrm{Re}V_s) \rvert / A$	$\lvert I(\mathrm{Im}V_s) \rvert / A$	A
		(MeV - 10^{-39} cm^3)				(amu)
He	Gaussian	- 34	281	9	32	4.003
Be	Mod. Gauss.	- 52	294	6	21	9.013
C	Mod. Gauss.	- 57	330	8	22	12.011
C	Fermi	- 56	325	7	23	12.011
Al	Fermi	- 56	316	6	20	26.98
Ca	Fermi	- 55	313	8	12	40.08
Fe	Fermi	- 55	312	7	17	55.85
Ta	Fermi	- 54	309	7	22	180.95

Element	Model	f	$a_1/A_{1/3}$	a	$r_0/A_{1/3}$	$\bar{\sigma}$	σ_t	σ_a
			(10^{-13} cm)			(mb)		
He	Gaussian	0.0	0.93 ± .02	-	-	39 ± 3	116	90
Be	Mod. Gauss.	0.5	0.82 ± .02	-	-	38 ± 3	251	192
C	Mod. Gauss.	1.0	0.73 ± .02	-	-	42 ± 3	324	235
C	Fermi	-	-	0.50	0.98	42 ± 3	334	244
Al	Fermi	-	-	0.60	1.00	42[a]	649	454
Ca	Fermi	-	-	0.57	1.06	42[a]	891	598
Fe	Fermi	-	-	0.57	1.06	42[a]	1121	729
Ta	Fermi	-	-	0.64	1.14	42[a]	2813	1690

[a] Held fixed during analysis

FIGURE LEGENDS

Fig. 1. Beam layout.

Fig. 2. Beam profiles after spectrometer for protons double-scattering from carbon for (a) θ_1 = 3 deg, and (b) θ_1 = 13 deg. Counter 6 is on the high-energy side. Each counter subtends 5 MeV. The increased spread in (b) is due to the greater proportion of near-elastic scatterings produced at the larger angle.

Fig. 3. (a) Differential cross section and (b) polarization vs energy from protons on carbon at 6 deg (lab). ▼ , Ref. 8; ○ Ref. 9; ● Ref. 10; Δ , Ref. 4; ▲ , Ref. 11; □ Ref. 12 (scaled down from 6.33 deg); ◆ , Ref. 13; ■ , this experiment; ▽ , Ref. 5 (extrapolated).

Fig. 4. Differential cross section and polarization vs angle for protons on protons. The upper (▲) and lower (▼) sets of polarization points are derived from Curves A and B respectively on Fig. 3. The error bars on the cross sections include the 5% reproducibility error but not the uncertainty in the p-C cross section.

Fig. 5. Maximum pp polarization as a function of energy. ● , Ref. 14; □ , Ref. 15; ■ , Ref. 16; ▲ , Ref. 17; ▽ , Ref. 7; ◆ , this experiment (A and B refer to the choice of values for p-C polarization, Fig. 3b); ▽ , Ref. 18.

Fig. 6. Differential cross section and polarization vs angle for protons on helium. The curves are the result of the optical model for elastic scattering, with the potentials and radial values given in Table IV.

Δ Includes elastic events only

□ Includes inelastic events to about 30 MeV loss.

Fig. 7. Differential cross section and polarization vs angle for protons on beryllium. The curves are the result of the optical model for elastic scattering, with the potentials and radial values given in Table IV.

□ Includes inelastic events to about 15 MeV loss

Δ Includes inelastic events to about 30 MeV loss.

Fig. 8. Differential cross section and polarization vs angle for protons on carbon. The curves are the result of the optical model for elastic scattering, with the potentials and radial values given in Table IV.

□ Includes inelastic events to about 15 MeV loss

Δ Includes inelastic events to about 30 MeV loss.

Fig. 9. Differential cross section and polarization vs angle for protons on aluminum. The curves are the result of the optical model for elastic scattering, with the potentials and radial values given in Table IV.

□ Includes inelastic events to about 15 MeV loss

Δ Includes inelastic events to about 30 MeV loss.

Fig. 10. Differential cross section and polarization vs angle for protons on calcium. The curves are the result of the optical model for elastic scattering, with the potentials and radial values given in Table IV.

□ Includes inelastic events to about 15 MeV loss

Δ Includes inelastic events to about 30 MeV loss.

Fig. 11. Differential cross section and polarization vs angle for protons on iron. The curves are the result of the optical model for elastic scattering, with the potentials and radial values given in Table IV.

□ Includes inelastic events to about 15 MeV loss

Δ Includes inelastic events to about 30 MeV loss.

Fig. 12. Differential cross section and polarization vs angle for protons on tantalum. The curves are the result of the optical model for elastic scattering, with the potentials and radial values given in Table IV.

□ Includes inelastic events to about 15 MeV loss

Δ Includes inelastic events to about 30 MeV loss.

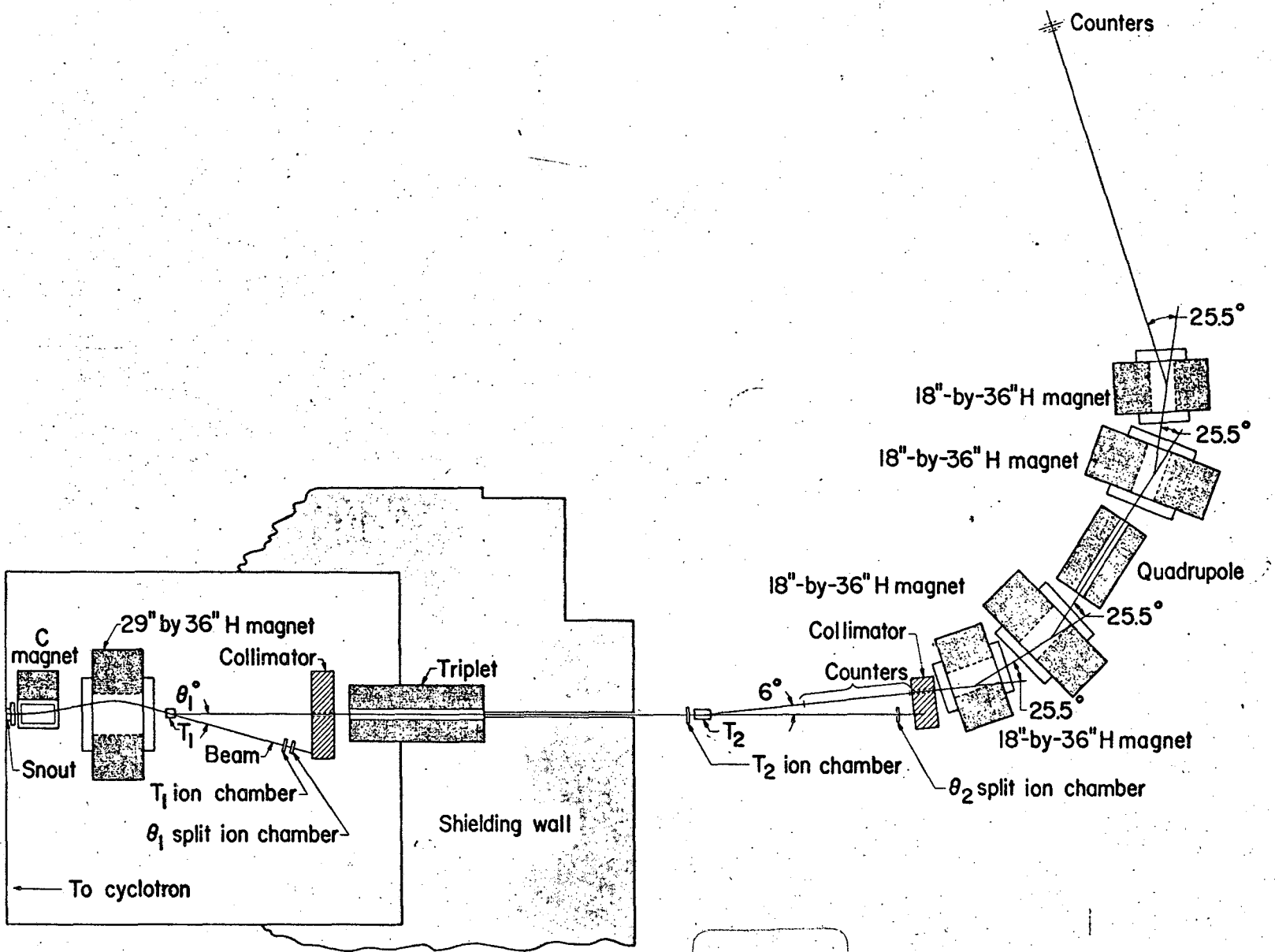

Fig. 1

UCRL-11496

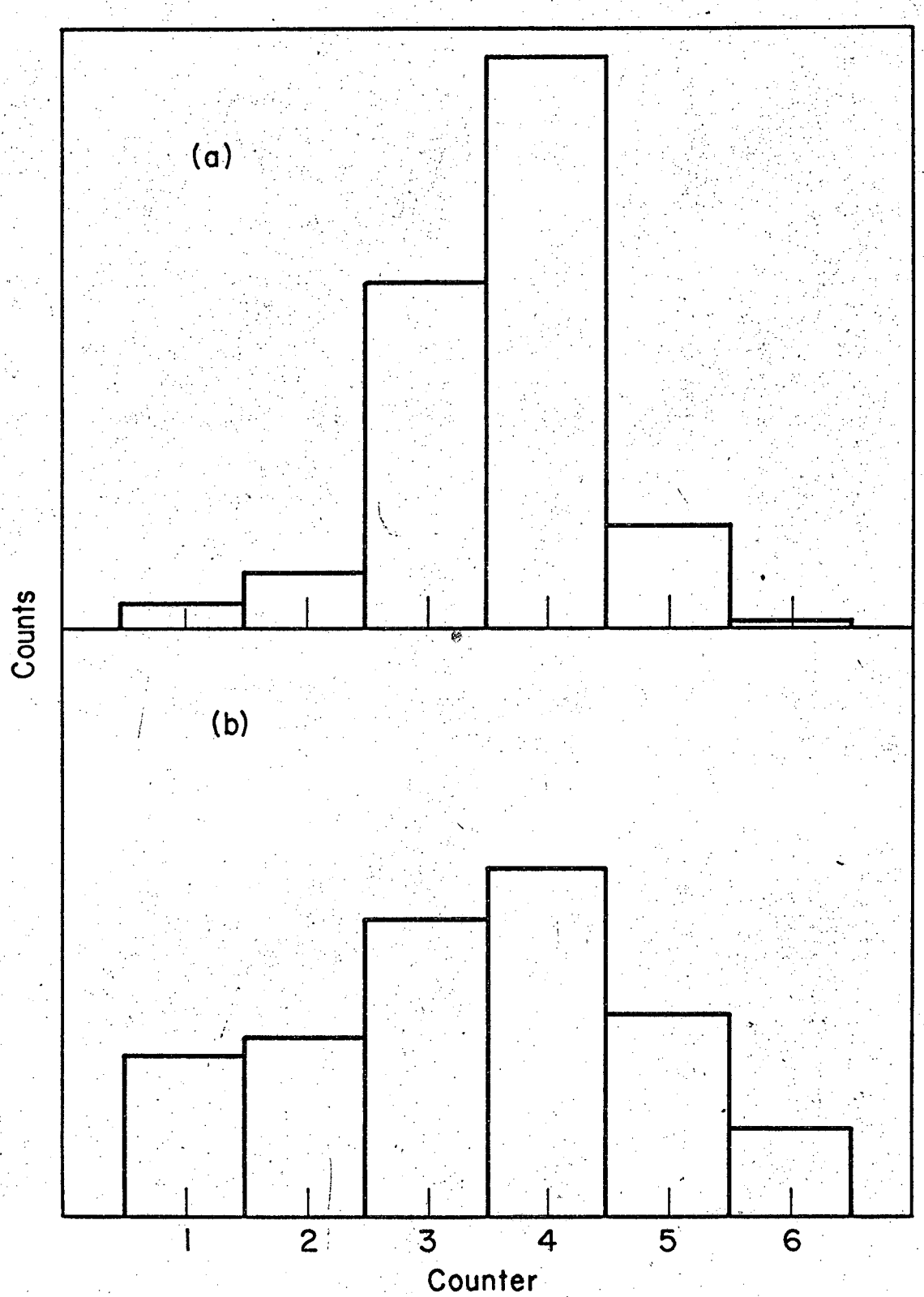

Fig. 2

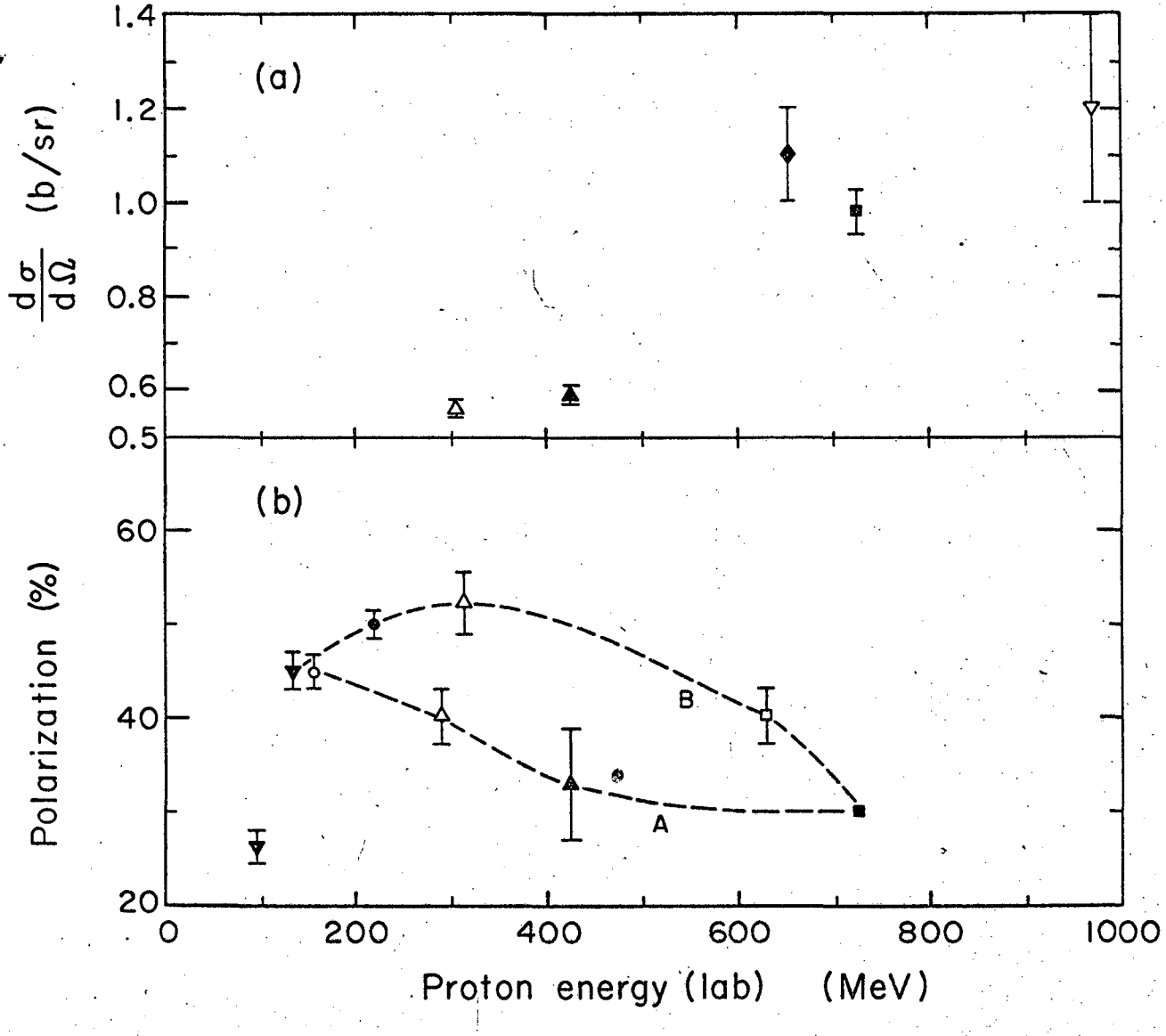

Fig. 3

MUB-3881

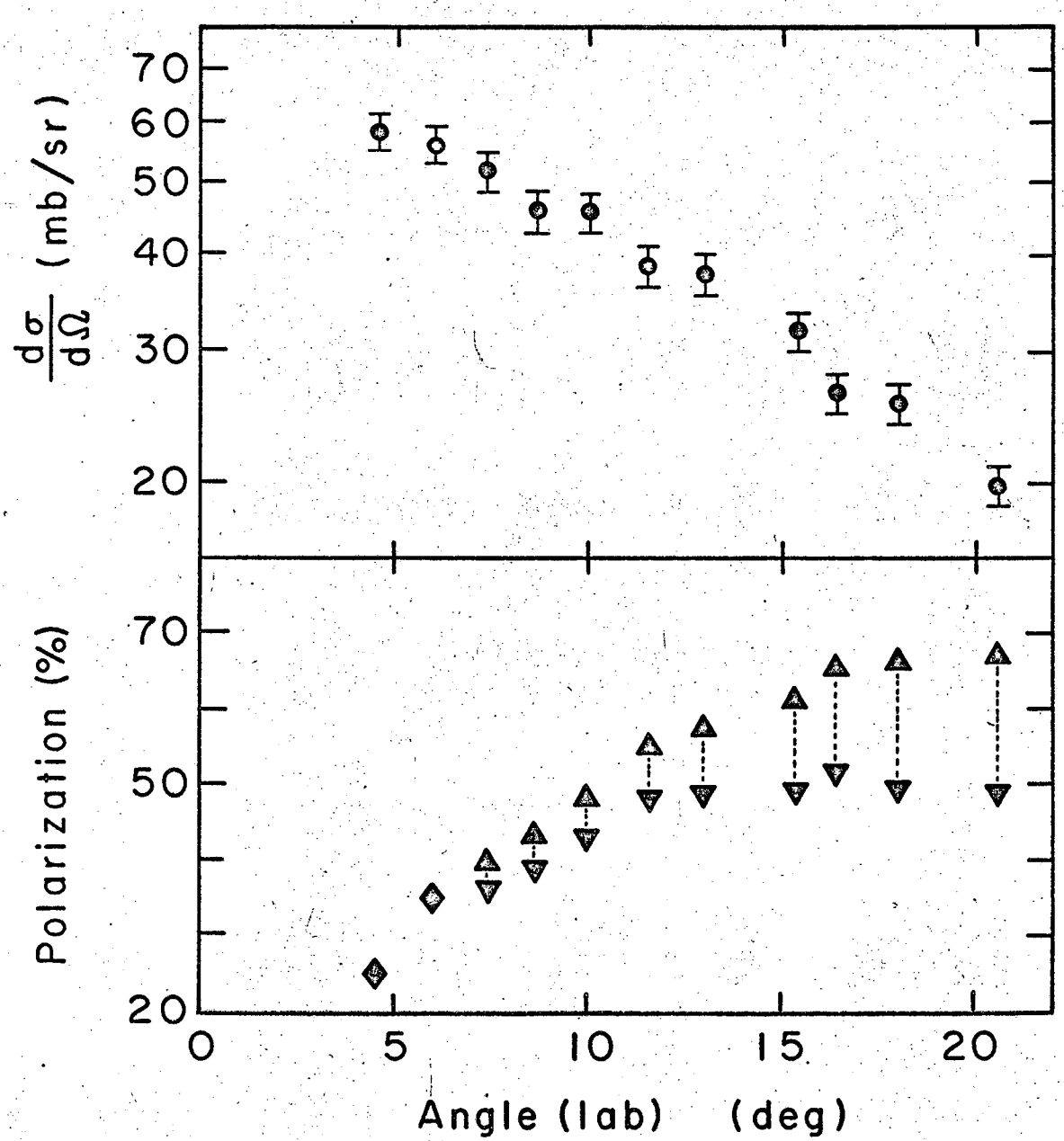

Fig. 4

MUB-3882

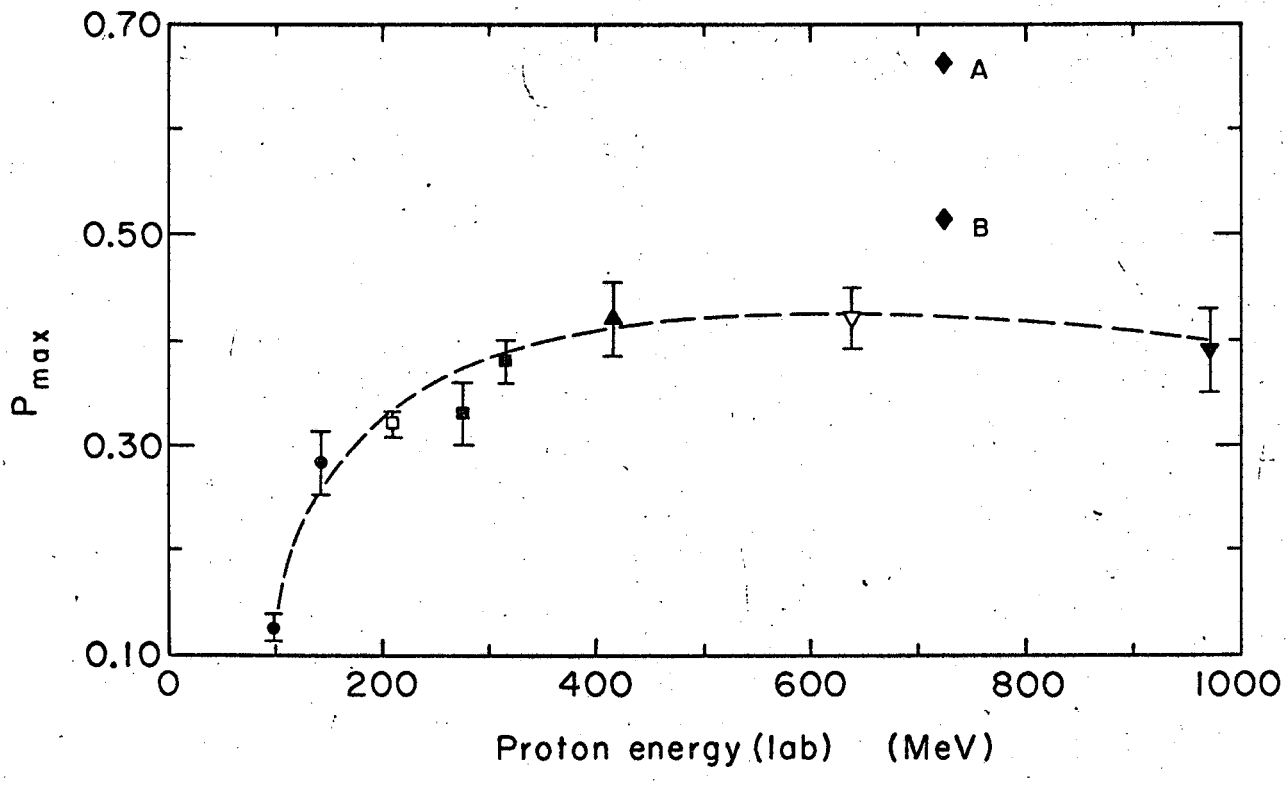

MUB-3883

Fig. 5

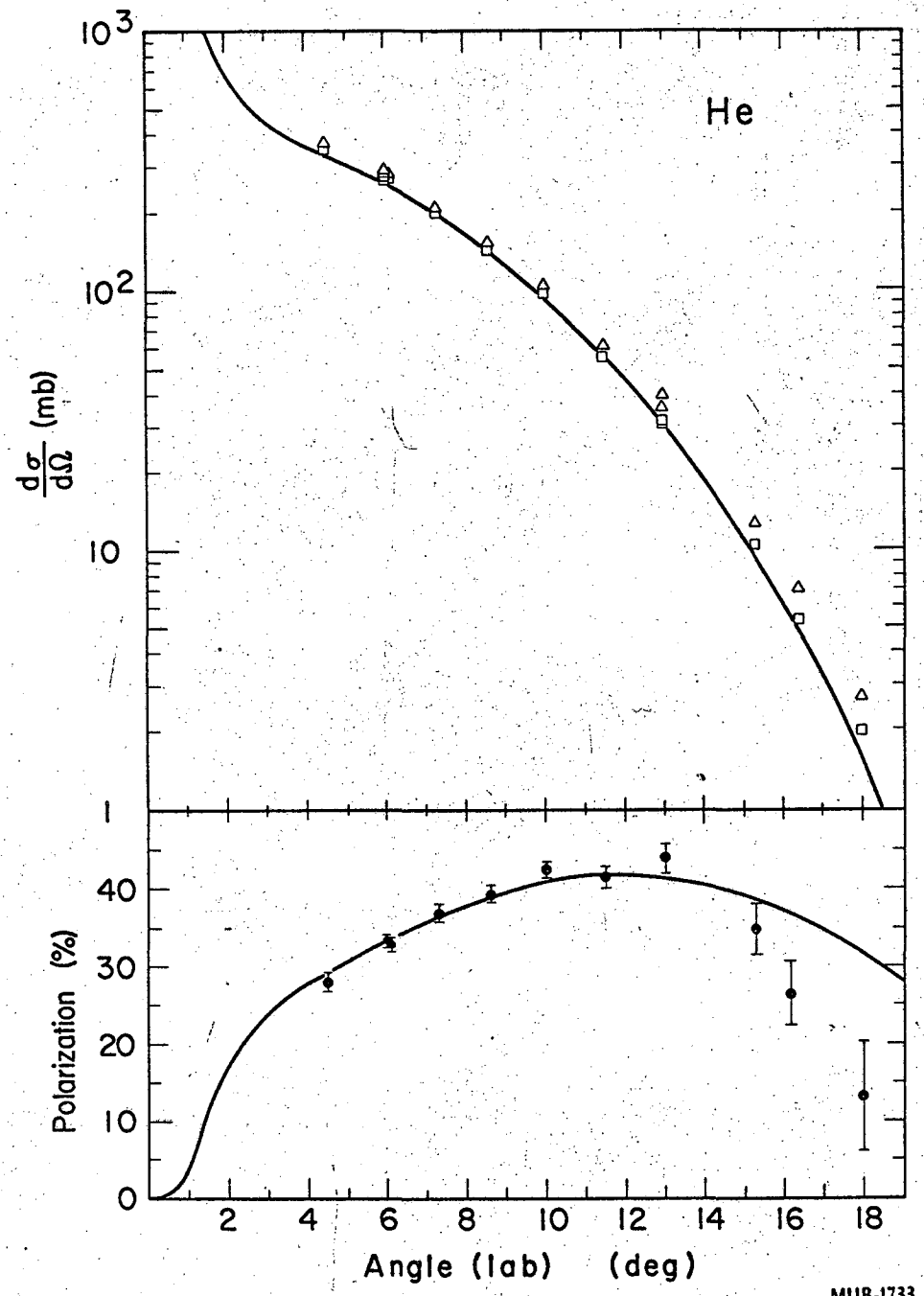
He
10^3
10^2
10
1
$\frac{d\sigma}{d\Omega}$ (mb)
Polarization (%)
40
30
20
10
0
2
4
6
8
10
12
14
16
18
Angle (lab) (deg)
MUB-1733

Fig. 6

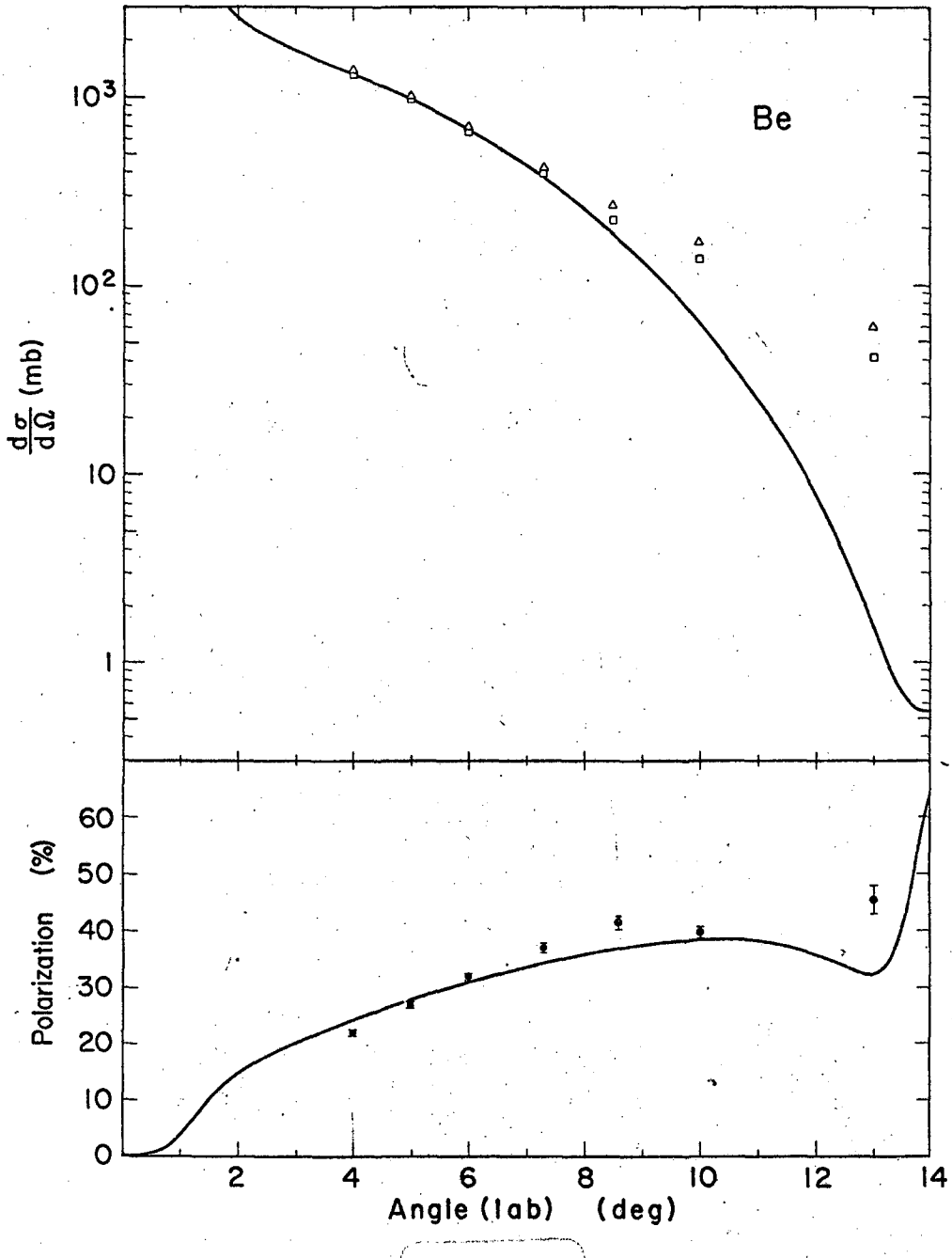
Be
$\frac{d\sigma}{d\Omega}$ (mb)
10^3
10^2
10
1
Polarization (%)
60
50
40
30
20
10
0
2
4
6
8
10
12
14
Angle (lab) (deg)
MUB-1738

Fig. 7

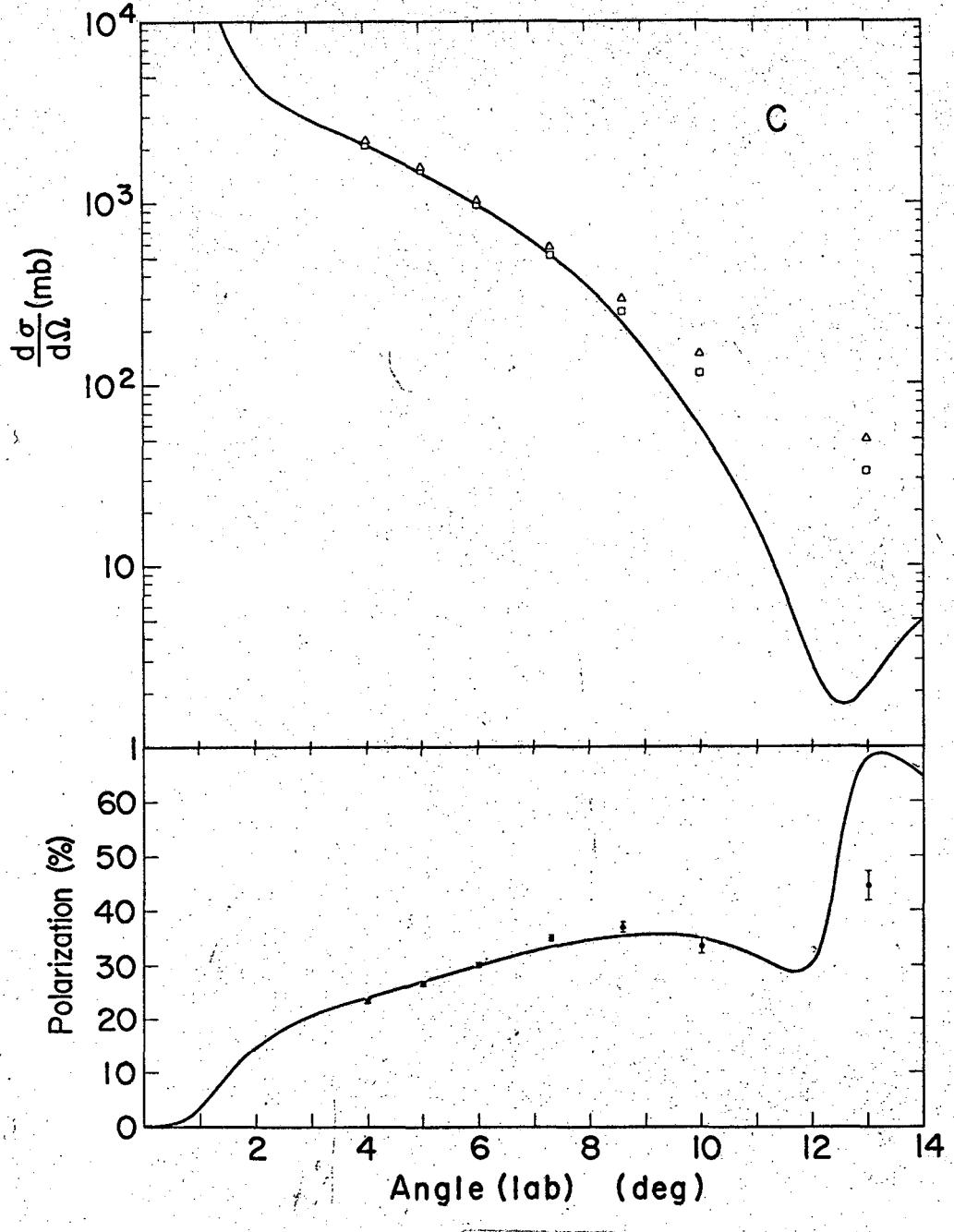
C
$\frac{d\sigma}{d\Omega}$ (mb)
10^4
10^3
10^2
10
1
Polarization (%)
60
50
40
30
20
10
0
2
4
6
8
10
12
14
Angle (lab) (deg)
MUB-1739

Fig. 8

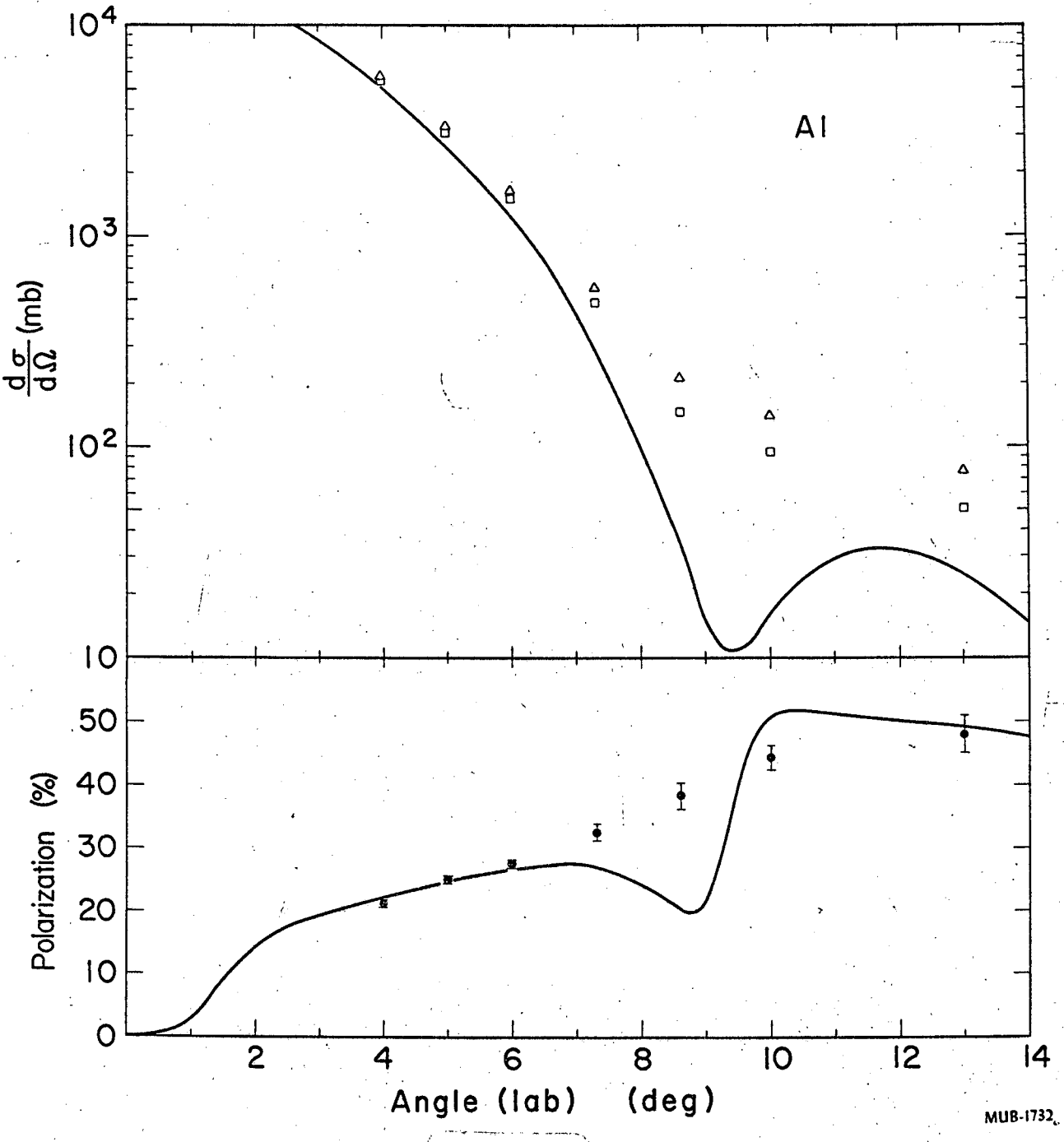
Al
$\frac{d\sigma}{d\Omega}$ (mb)
10^4
10^3
10^2
10
Polarization (%)
50
40
30
20
10
0
2
4
6
8
10
12
14
Angle (lab) (deg)
MUB-1732

Fig. 9

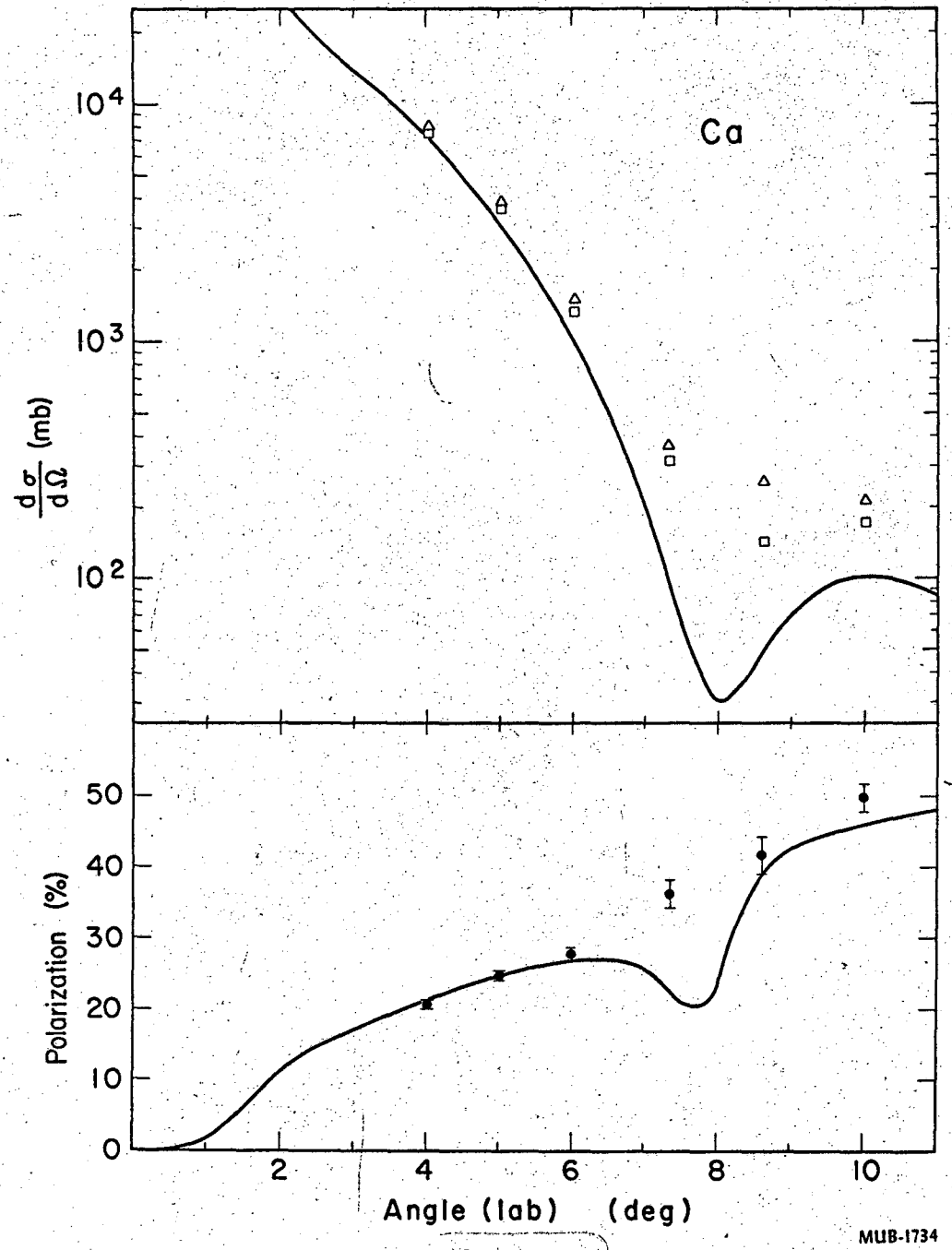
Ca
10^4
10^3
10^2
$\frac{d\sigma}{d\Omega}$ (mb)
50
40
30
20
10
0
Polarization (%)
2
4
6
8
10
Angle (lab) (deg)
MUB-1734

Fig. 10

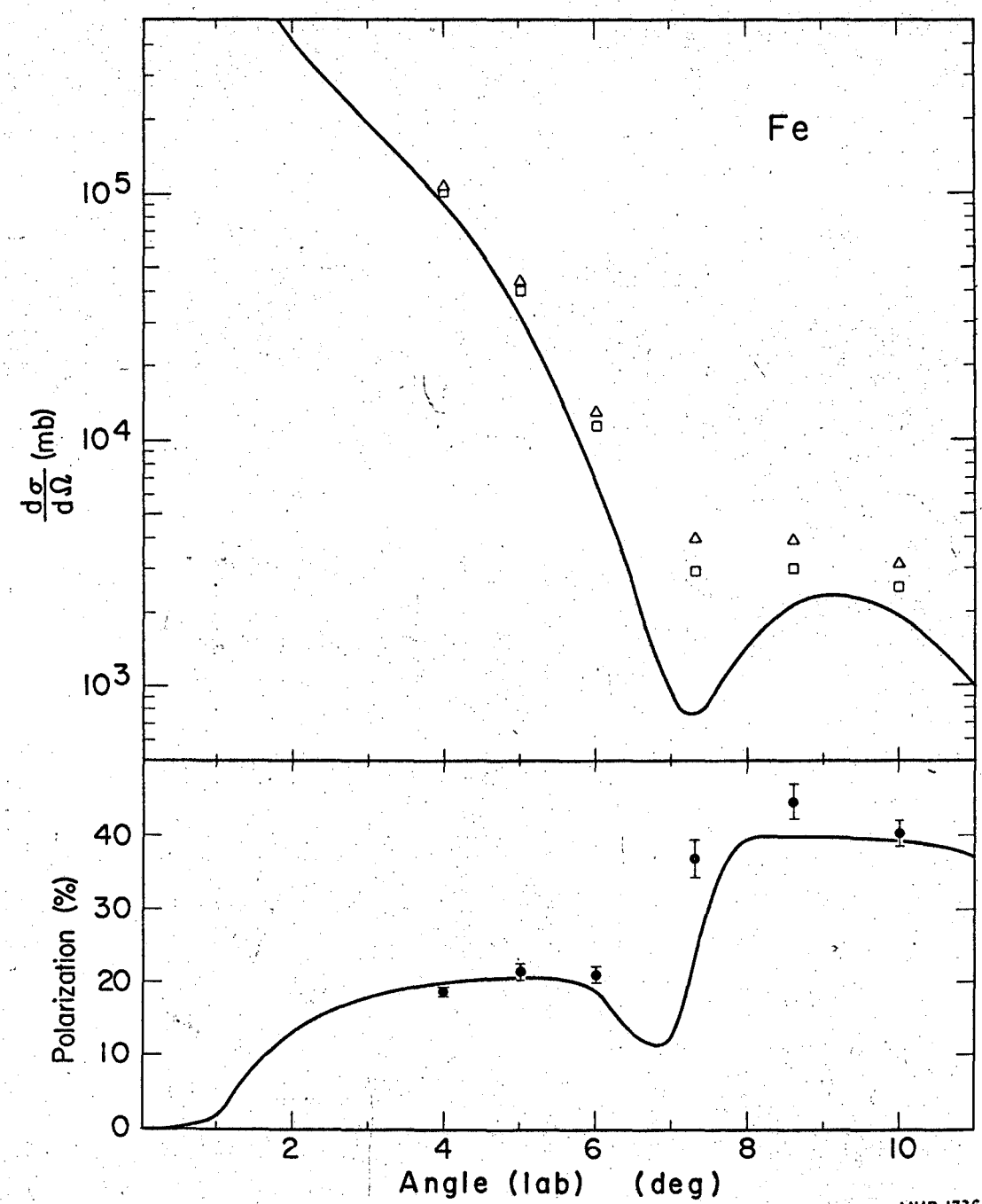
Fe
10^5
10^4
10^3
$\frac{d\sigma}{d\Omega}$ (mb)
40
30
20
10
0
Polarization (%)
2
4
6
8
10
Angle (lab) (deg)
MUB-1736

Fig. 11

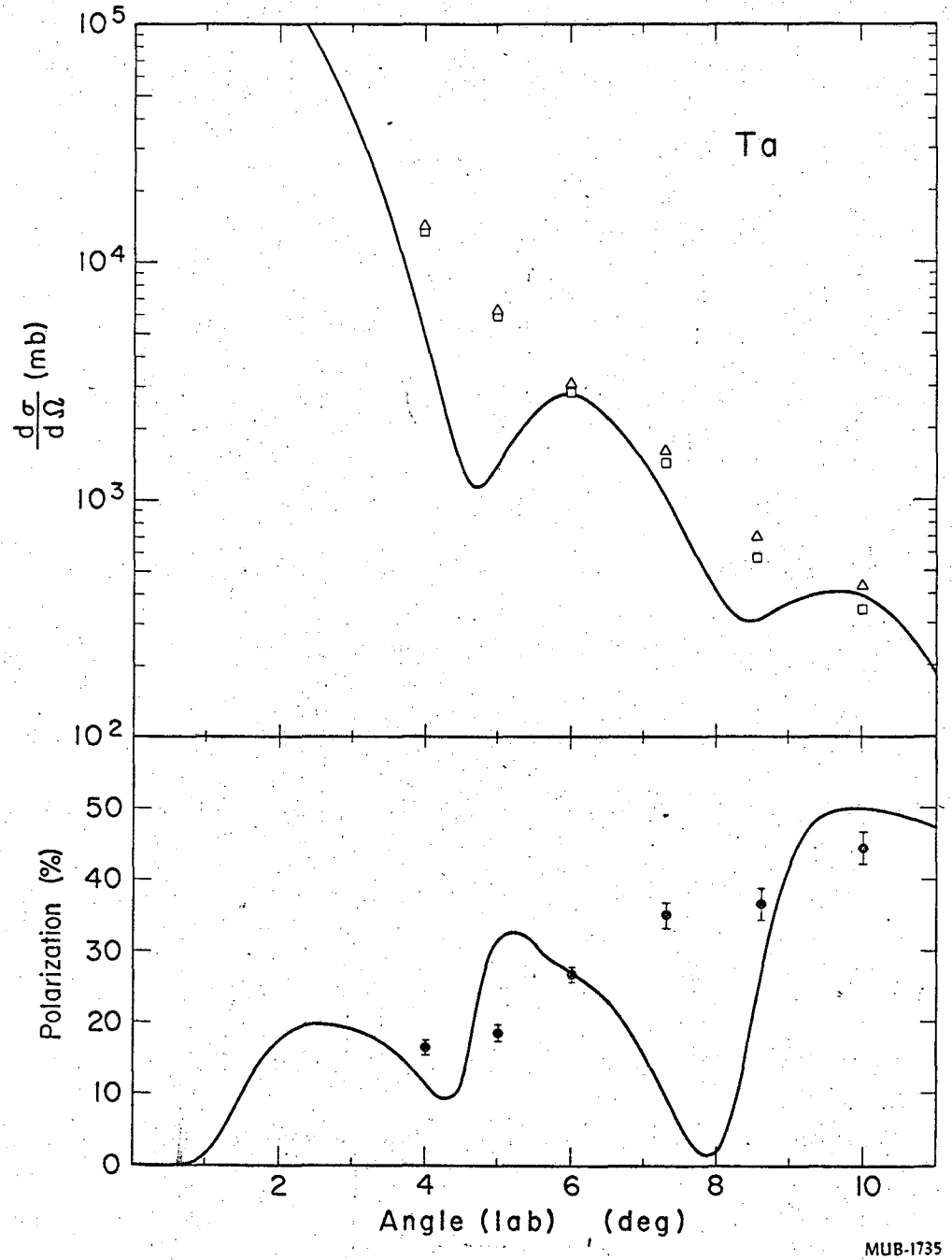
Ta
$\frac{d\sigma}{d\Omega}$ (mb)
10^5
10^4
10^3
10^2
Polarization (%)
50
40
30
20
10
0
2
4
6
8
10
Angle (lab) (deg)
MUB-1735

Fig. 12